www.czasopisma.pan.pl PAN www.journals.pan.pl
POLSKA AKADEMIA NAUK

Arch. Metall. Mater. **67** (2022), 3, 815-825

DOI: https://doi.org/10.24425/amm.2022.139671

SHIH-HSIEN CHANG[1*], CHEN-YU WENG[1], KUO-TSUNG HUANG[2], CHENG LIANG[1]

INVESTIGATION OF THE MICROSTRUCTURE AND STRENGTHENING MECHANISMS OF Ti-6Cu-8Nb-xCr_3C_2 ALLOY THROUGH VACUUM SINTERING PROCESS

This study mixes four different powders to produce Ti-6Cu-8Nb-xCr_3C_2 (x = 1, 3, and 5 mass%) alloys in three different proportions. The experimental results reveal that when 5 mass% Cr_3C_2 was added to the Ti-6Cu-8Nb alloys, the specimen possessed optimal mechanical properties after sintering at 1275°C for 1 h. The relative density reached 98.23%, hardness was enhanced to 67.8 HRA, and the transverse rupture strength (TRS) increased to 1821.2 MPa, respectively. The EBSD results show that the added Cr_3C_2 in situ decomposed into TiC and NbC during the sintering process, and the generated intermetallic compounds (Ti_2Cu) were evenly dispersed in the Ti matrix. Furthermore, the reduced Cr atom acts as a β-phase stabilizing element and solid-solution in the Ti matrix. Consequently, the main strengthening mechanisms of the Ti-6Cu-8Nb-xCr_3C_2 alloys include dispersion strengthening, solid-solution strengthening, and precipitation hardening.

Keywords: vacuum sintering; Ti-6Cu-8Nb-Cr_3C_2 alloy; hardness; transverse rupture strength; EBSD

1. Introduction

Recently years, titanium (Ti) and titanium alloys are widely used in medical implants due to their good physicochemical properties and biocompatibility. They are mainly used in the field of joint prosthesis and dental implants [1-3]. J.P. Oliveira et al also reported that the functional properties of titanium alloys such as NiTi and Ti6Al4V are of significant interest in a wide range of industries including medical, aerospace and seismic damping devices [4-6]. Moreover, copper (Cu) is a necessary trace element in the human body, and also a well-known metal element with antimicrobial ability. By proper addition of Cu element into currently used metallic biomaterials, the materials are expected to possess excellent antibacterial properties [7]. The key factors controlling mechanical, antibacterial and corrosion resistance properties of Ti-Cu alloys should be both Cu content and microstructure [8,9].

In addition, the low Young's modulus (it is worth noting that the young's modulus varies significantly depending on the composition) Ti alloys have been developed with better mechanical properties, good corrosion resistance and excellent biocompatibility, by using β-stabilizer and biocompatible elements such as Nb, Mo, Ta, Zr, especially for orthopedic implant applications [10]. Among these alloys, Ti-Nb-based metastable titanium alloys are among the most promising candidates for long-term implantation [11,12]. E. Yılmaz et al also indicated Ti-Nb alloys with the properties of low elastic modulus, high strength and good biocompatibility. This alloys draw a considerable attention for biomedical applications not only due to their nontoxicity and biocompatibility, but also due to the presence of Nb that is reported as favorable for osteogenesis, cell adhesion and proliferation [10,13-15].

Metal matrix composites (MMCs) are being applied increasingly widely in many branches of modern industry, such as the automotive, military and aerospace industries, especially where there is required excellent mechanical properties and corrosion resistance [16,17]. In the past two decades, titanium matrix composites (TMCs) reinforced with ceramic particles have received considerable attention due to their high specific strength and specific stiffness, good chemical resistance, as well as promising mechanical properties [18]. Whereby, they have been widely applied in many fields, such as advanced military, aerospace, automotive and biomedical applications. Furthermore, by adding a grain growth inhibitor such as VC, Cr_3C_2 or NbC has been found to effectively control grain coarsening during sintering and improve the mechanical properties of titanium matrix composites. Among them, chromium carbide (Cr_3C_2) is the most effective grain growth inhibitor due to its high solubility

[1] NATIONAL TAIPEI UNIVERSITY OF TECHNOLOGY, DEPARTMENT OF MATERIALS AND MINERAL RESOURCES ENGINEERING, TAIPEI 10608, TAIWAN, ROC
[2] NATIONAL KANGSHAN AGRICULTURAL INDUSTRIAL SENIOR HIGH SCHOOL, DEPARTMENT OF AUTO-MECHANICS, KAOHSIUNG 82049, TAIWAN, ROC

* Corresponding author: changsh@ntut.edu.tw

© 2022. The Author(s). This is an open-access article distributed under the terms of the Creative Commons Attribution-NonCommercial License (CC BY-NC 4.0, https://creativecommons.org/licenses/by-nc/4.0/deed.en which permits the use, redistribution of the material in any medium or format, transforming and building upon the material, provided that the article is properly cited, the use is noncommercial, and no modifications or adaptations are made.

and mobility in the metal matrix phase [19,20]. The widely accepted inhibition mechanism of Cr_3C_2 is related to its ability to slow solution/re-precipitation reactions during the liquid phase sintering (LPS) of the powder metallurgy (PM) process [20,21].

Generally speaking, PM methods offer two or more different materials with a view to achieving lightweight, high strength, hardness and wear resistance properties [22]. PM fabrication process can produce complex-shaped Ti alloy components to avoid material loss [3]. As mentioned previously, while Ti-Cu and Ti-Nb alloys possess superior properties and have recently been widely researched, Ti-Cu-Nb alloys have not been further studied or reported. Besides, our previous studied found that the 8 mass% Nb added to Ti-Cu alloy can achieve good mechanical properties. Therefore, the study first conducted the research on Ti-6Cu-8Nb alloys and attempted to find the optimal sintering parameters of this alloys. Furthermore, in order to further improve the microstructure and mechanical properties of the Ti-6Cu-8Nb alloys, this paper referred to our previous studies and added the 1, 3 and 5 mass% of Cr_3C_2 to Ti-6Cu-8Nb alloys [2,3]. However, how to produce a novel material with the better hardness and strength of Ti-6Cu-8Nb-xCr_3C_2 composites is an important research topic. Moreover, it is still unclear whether Ti-6Cu-8Nb alloys with different amounts of Cr_3C_2 particles in the strengthening phase can obtain better mechanical properties, or good corrosion resistance for Ti-6Cu-8Nb-xCr_3C_2 composites after vacuum sintering using the PM technique. In order to examine the effects on the microstructure and mechanical properties of Cr_3C_2-strengthened Ti-6Cu-8Nb alloys, this study aims to explore a series of vacuum sintering processes for Ti-6Cu-8Nb-xCr_3C_2 composites, and examine the effects on the microstructure, mechanical properties, and corrosion behaviors of Cr_3C_2-strengthened Ti-6Cu-8Nb alloys.

2. Experimental Procedures

This experiment first used three different powders (titanium, copper, and niobium), which were mixed to produce three different proportions of Ti-6Cu-xNb alloys (8, 10 and 12 mass% Nb). Here the ratio of adding Nb and the setting of process parameters are based on our previous research [2,3]. The Ti-6Cu-xNb alloys underwent a vacuum sintering process at temperatures of 1175°C, 1200°C, 1225°C, and 1250°C for 1 h, and the experimental results reveal that Ti-6Cu-8Nb alloys sintered at 1225°C for 1 h possessed the optimal mechanical properties. The relative density reached 95.03%, the hardness was 62.8 HRA, and the transverse rupture strength (TRS) was 1517.6 MPa, respectively. In order to further improve the sintering density and properties of the Ti-6Cu-8Nb alloys, this study utilized Ti-6Cu-8Nb alloy powders and added different ratios of refined Cr_3C_2 powders as a strengthening element to explore the effects of a series of vacuum sintering processes.

In this research, the mean particle sizes of Ti, Cu, Nb, and Cr_3C_2 powders were about 31.3±1.5, 4.5±0.5, 14.9±0.5, and 3.8±0.5 μm, respectively. Meanwhile, the morphology of the Ti reduced powders showed an irregularly shaped surface, the Cu powders possessed a nearly round appearance, and Nb and Cr_3C_2 displayed an irregularly shaped and polygonal appearance. In addition, the different amounts of Cr_3C_2 powders (1, 3 and 5 mass%) were mixed and added to Ti-6Cu-8Nb-xCr_3C_2 alloy powders, hereafter, designated as 1 Cr_3C_2, 3 Cr_3C_2, and 5 Cr_3C_2. The mixing experiment utilized a three-degree space rotary mixer (Turbula Shaker-Mixer, T_2C). In addition, the mixed powders were further analyzed by XRD technique, and no other chemical elements or impurities were found in this study. After milling, PVA (polyvinyl alcohol) was added as a binder, and the green compact (40 × 6 × 6 mm^3) of the powder specimen was produced under uniaxial pressure at 350 MPa for 300 s.

To evaluate the effects of microstructure evolution on the Ti-6Cu-8Nb-xCr_3C_2 alloys *via* vacuum sintering process, this study conducted volume shrinkage, apparent porosity, relative density, mean grain size, hardness, TRS tests, XRD (Bruker/D2 Phaser) analysis, Optical Microscopy (OM, Nikon optiphot 66), Scanning Electron Microscopy (SEM, Hitachi-S4700) and Electron Backscatter Diffraction (EBSD, JSM-7800F) microstructure observations. Porosity test was conducted in accordance to the ASTM C373-88 standard. Hardness tests were measured by HRA with a loading of 588 N, which followed the ASTM E18-3 standard. Furthermore, the Hung Ta universal material test machine (HT-9501A) with a maximum load of 25 tons was used for TRS tests (ASTM B528-05). The TRS was obtained by the equation $R_{bm} = 3FLk/2bh^2$, where R_{bm} is the TRS, which is determined as the fracture stress in the surface zone, F is maximum fracture load. In this work, L was 30 mm, k was chamfer correction factor (normally 1.00-1.02), b and h were 5 mm, respectively. The specimen dimensions of the TRS test were 5 × 5 × 40 mm^3 and tests at least three pieces.

In this work, corrosion potential (Potential Stat Chi 601) analysis uses three electrodes method and follows by ASTM G59-97: the reference electrode is a saturated of silver-silver chloride electrode, auxiliary electrode uses a platinum electrode, and the working electrode is connected to the test specimens [3]. The contact area of the specimen was 0.78 cm^2. The corrosive solvent used 1 N H_2SO_4 was maintained at room temperature. A scanning speed of 0.01 $V \cdot s^{-1}$, initial potential of –1.5 V, and the final potential of 3.5 V were controlled. The polarization curve was obtained by Corr-View software to analyze and compare the corrosion potential (E_{corr}), corrosion current (I_{corr}) and polarization resistance (R_p) of sintered Ti-6Cu-8Nb-xCr_3C_2 alloys.

3. Results and Discussion

3.1. Effect of Cr_3C_2 content and sintering temperature on the mechanical properties

Fig. 1 represents the volume shrinkage, apparent porosity, and relative density of the Ti-6Cu-8Nb-xCr_3C_2 alloys under different sintering temperatures. It was found that, as the Cr_3C_2 content (1 → 3 → 5 mass%) or the sintering temperature were

increased (1225 → 1250 → 1275 → 1300°C), the volume shrinkage increased gradually, as shown in Fig. 1a. When the sintering temperature reached 1300°C, all the specimens had relatively high-volume shrinkage; among them, the 5 Cr_3C_2 specimen sintered at 1300°C for 1 h possessed the highest volume shrinkage (29.58%). It is speculated that the Cr_3C_2 additive had a large elastic modulus (347 GPa), as indicated by the high rigidity, and thus, required greater stress to produce the plastic deformation of the composite specimens. As a result, the increased addition of Cr_3C_2 powders led to the larger embryo volume. When 5 mass% Cr_3C_2 was added, the volume shrinkage was slightly larger than 1 and 3 mass%. As seen in Fig. 1a, it was observed that, as the sintering temperature increased, the volume shrinkage had a tendency to increase significantly. This result is similar to the initial Ti-6Cu-8Nb alloy at the optimal sintering temperature (at 1250°C, the volume shrinkage was about 29.83%), meaning that the addition of Cr_3C_2 did not have a dramatic effect on the volume shrinkage of the Ti-6Cu-8Nb-xCr_3C_2 alloys.

Fig. 1b shows the apparent porosity of 1 Cr_3C_2, 3 Cr_3C_2, and 5 Cr_3C_2 specimens after different sintering temperatures for 1 h. It was found that the apparent porosity increased slightly as the Cr_3C_2 content increased (1 → 3 → 5 mass%) after sintering at 1225°C (1.05 → 1.59 → 2.61%) and 1250°C (0.88 → 0.93 → 0.99%); however, the apparent porosity tended to significantly decrease as the sintering temperature increased. Due to the addition of high-melting ceramic carbides in the experiment, the driving energy for sintering at 1225°C was insufficient, thus, when more Cr_3C_2 was added, it led to increased remaining pores. Moreover, the apparent porosity of all specimens were highest after sintering at 1225°C for 1 h. However, when the sintering temperature was increased to 1250°C, the porosity decreased significantly. Generally speaking, an increase in sintering temperature can enhance the thermal energy and extend the diffusion time [3]. This result reveals that increasing the sintering temperature can effectively increase the driving energy for Ti-6Cu-8Nb-xCr_3C_2 alloys. When the sintering temperature was increased to 1275°C, the apparent porosity slightly decreased with the increase of Cr_3C_2 content, and the apparent porosities of the 1 Cr_3C_2, 3 Cr_3C_2, and 5 Cr_3C_2 specimens were 0.84%, 0.81%, and 0.63% after sintering at 1275°C, respectively. It is worth noting that when the temperature exceeded 1275°C, the increase in the appropriate amount of Cr_3C_2 effectively helped to reduce the apparent porosity, which is beneficial to sintering densification. Therefore, the 5 Cr_3C_2 specimen possessed the lowest apparent porosity (0.11%) after 1300°C sintering for 1 h.

The relative densities of the 1 Cr_3C_2, 3 Cr_3C_2, and 5 Cr_3C_2 specimens after the different sintering temperatures for 1 h are shown in Fig. 1b, where it can be observed that the relative density is inversely proportional to the apparent porosity. As previously mentioned, the Ti-6Cu-8Nb-xCr_3C_2 specimens require a higher temperature to achieve complete densification, thus, when the sintering temperature is increased to 1250°C, its relative density is significantly increased. All the composite specimens have higher relative density than that of Ti-6Cu-8Nb alloys (95.03%), which shows that adding Cr_3C_2 to the Ti-6Cu-8Nb alloy in the range of 1250°C~1300°C is effective in improving the sintering densification. In this present research, while the 5 Cr_3C_2 specimen sintered at 1300°C possessed the highest relative density (99.33%), the 3 Cr_3C_2 specimens sintered at 1300°C and 5 Cr_3C_2 specimens sintered at 1275°C also had good relative density (>98%). Moreover, the porosity levels of the 3 Cr_3C_2 and 5 Cr_3C_2 specimens were less than 1% after sintering at 1275 and 1300°C, respectively. In other words, the near-full theoretical sintered density of the Ti-6Cu-8Nb-xCr_3C_2 alloys was acquired. Consequently, the addition of Cr_3C_2 not only enhanced the volume shrinkage of Ti-6Cu-8Nb-xCr_3C_2 alloys, it also improved the relative density and apparent porosity by adding the appropriate content of Cr_3C_2.

Fig. 2 shows the XRD patterns of various amounts of mass% Cr_3C_2 added to Ti-6Cu-8Nb alloys after sintering at 1275°C for 1 h, and the results show that the main diffraction peaks are α-Ti, β-Ti, Ti_2Cu, TiC, and NbC. As previously mentioned, Cr_3C_2 in situ was reduced to Cr and C, and the decomposed C reacted with Ti to produce TiC (Cr_3C_2 + 2Ti → 2TiC + 3Cr).

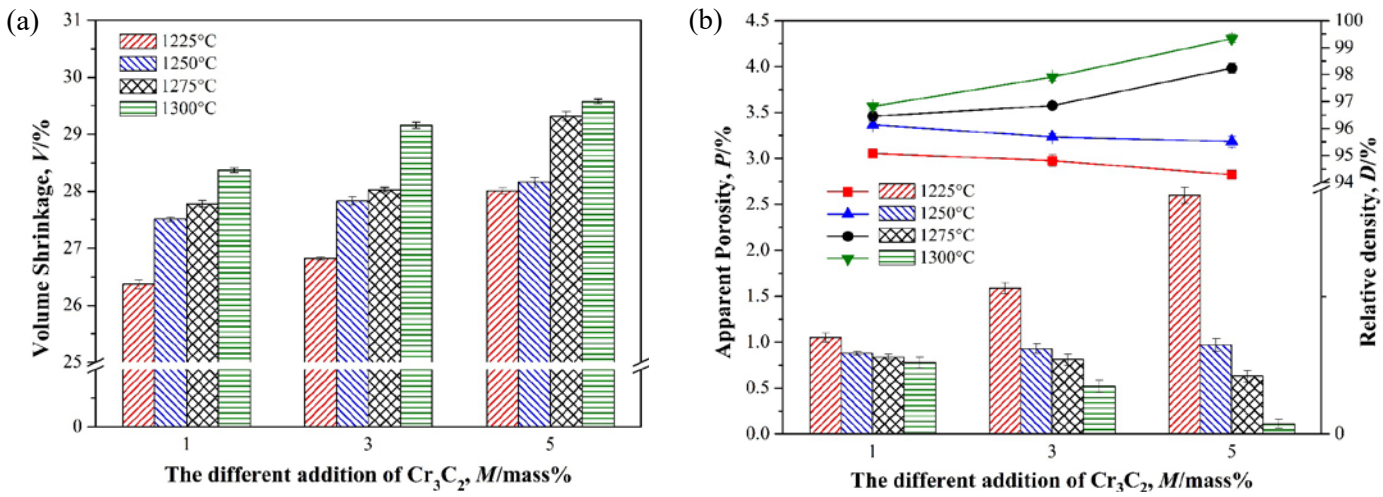

Fig. 1. Comparison of the (a) volume shrinkage, and (b) apparent porosity and relative density of various mass% Cr_3C_2 added to Ti-6Cu-8Nb alloys by the different sintering temperatures

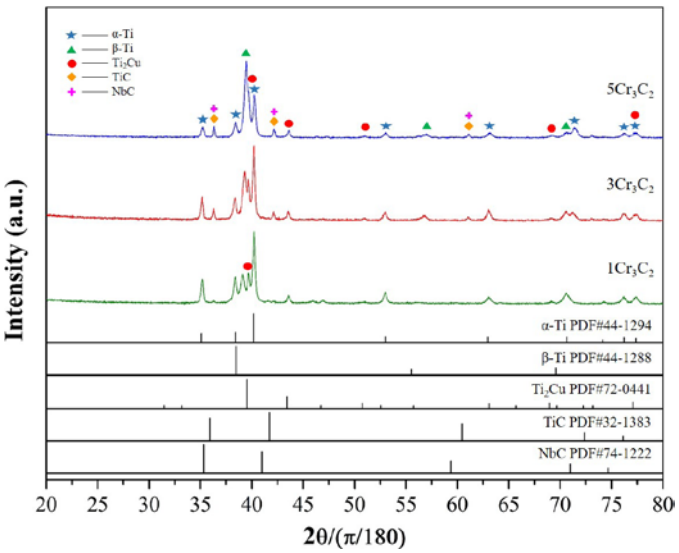

Fig. 2 XRD pattern of various mass% Cr_3C_2 added to Ti-6Cu-8Nb alloys after sintering at 1275°C for 1 h

This result verifies that the diffraction peak of TiC (PDF#32-1383) is enhanced with the increase of Cr_3C_2. The follow-up EDS and EBSD analysis will further prove that the diffraction peak of TiC was indeed transformed from Cr_3C_2. In addition, the results show that the diffraction peak of NbC (PDF#74-1222) overlapped with the diffraction peak of TiC. Whether or not there was NbC phase formation will be discussed in subsequent analysis. Since Cr was dissolved into the Ti matrix, it resulted in the Ti-6Cu-8Nb-xCr_3C_2 alloys producing a stable β-phase. Moreover, the small atomic radius of Cr (1.28Å) will effect and reduce the lattice constant of the β-phase, thus, with the increase of Cr_3C_2 (1 → 5 mass%), the diffraction peak of the α-phase can gradually be decreased and observed. The diffraction peak of the β-phase was simultaneously and significantly increased and shifted to higher angles, which shows the same trend at the sintering temperatures of 1225, 1250, and 1300°C. Furthermore, when the 5 Cr_3C_2 samples were sintered at the temperature range of 1250-1300°C, the intensity of the diffraction peak of the β-phase had a significant increase. This result indicates that the enhanced sintering temperature helped to promote the solid-solution of β-phase stabilizing elements, and fully dissolved the reduced Cr into β-Ti. As a result, more β-phase was retained to room temperature, and formed a metastable β-type of the Ti alloy.

Fig. 3a shows the hardness test results of the Ti-6Cu-8Nb-xCr_3C_2 specimens for different sintering temperatures. The hardness of the Ti-6Cu-8Nb-xCr_3C_2 specimens was obviously enhanced as the amount of added Cr_3C_2 was increased. At the same time, the hardness increased significantly as the sintering temperature was increased. Our previous research indicated that decreasing the porosity and increasing the density of sintered materials could effectively enhance plastic deformation resistance and hardness [2,3,16,17]. As seen in Fig. 3a, compared with the hardness of the Ti-6Cu-8Nb samples (63.5 HRA), the addition of 1 mass% Cr_3C_2 only slightly increased the hardness for Ti-6Cu-8Nb-xCr_3C_2 specimens after 1275 and 1300°C sintering for 1 h. It is reasonable to suggest that the Cr_3C_2 content (1 mass%) of the strengthening phase was not sufficient, thus, the effect of dispersion strengthening was limited. When the amount of Cr_3C_2 addition was increased to 3 and 5 mass%, it began to have an obvious strengthening effect. It is possible that the solid-solution of Cr increased the stability of the β-phase, thus, forming more ductile β-phases. Moreover, the in situ reaction (Cr_3C_2 + 2Ti → 2TiC + 3Cr) produced a large amount of TiC and NbC, which precipitates in the grain boundaries and can effectively prevent dislocation movement to achieve the strengthening effects. As a result, the 5 Cr_3C_2 specimen had the highest hardness (68.2 HRA) after 1300°C sintering for 1 h. Moreover, the 5 Cr_3C_2 specimen also had good hardness after 1275°C sintering for 1 h, and the hardness value was 67.8 HRA. This result is coherent with our previous research. While, the TiC and NbC precipitates will be confirmed in the subsequent EBSD analysis of this paper.

Fig. 3b shows the TRS values of Ti-6Cu-8Nb-xCr_3C_2 specimens after various sintering temperatures. Notably, the TRS value of Ti-6Cu-8Nb-xCr_3C_2 specimens had a tendency

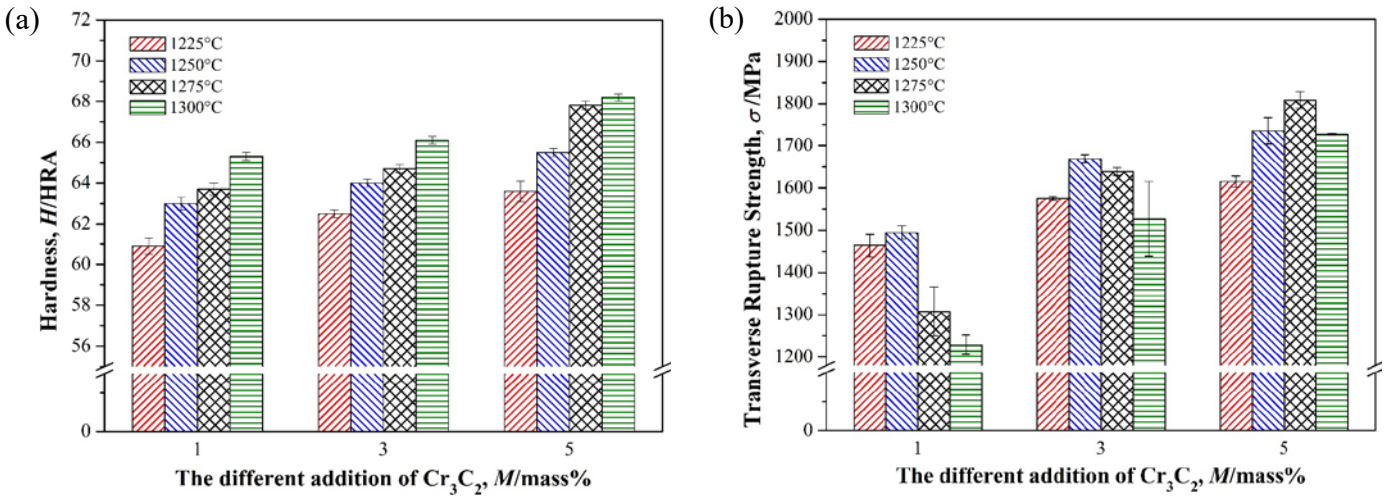

Fig. 3. Comparison of the hardness and TRS of various mass% Cr_3C_2 added to Ti-6Cu-8Nb alloys after sintering at 1275°C for 1 h: (a) hardness, and (b) TRS

to first rise, and then, decline as the sintering temperature was increased. However, the TRS increased with the increased addition of Cr_3C_2 at the same sintering temperature. Literature indicates the solid-solution of Cr in the Ti alloy, which increases the strength by about 65 MPa/mass% [23], thus, the solid-solution of Cr also has the effect of greatly improving strength. As the sintering temperature is increased, the porosities decrease (as seen in Fig. 1b), while the amount of carbide precipitates increase, thus, the strength also increases. Moreover, when the sintering temperature was increased to 1275°C, it was observed that the TRS values of the 1 Cr_3C_2 and 3 Cr_3C_2 specimens were not increased, but decreased. It is speculated that, due to the addition of a small amount of Cr_3C_2, the effect of inhibiting grain growth was limited. Meanwhile, the 1 Cr_3C_2 and 3 Cr_3C_2 specimens produced a coarsening phenomenon after 1275°C sintering for 1 h (the mean grain sizes were 67.37 and 60.12 μm, respectively), which reduced the TRS. Conversely, the mean grain size of 1275°C sintered – 5 Cr_3C_2 specimens dramatically decreased to 48.28 μm, which resulted in the higher TRS. This result clearly shows that adding 5 mass% Cr_3C_2 has the best effect on inhibiting grain growth.

In this work, the solid-solution reaction of the Cr elements of 5 Cr_3C_2 specimens possessed lower apparent porosity, more β-phase fractions, and a large amount of precipitated carbides, which inhibited grain growth after 1275°C sintering for 1 h. Hence, the 1275°C sintered – 5 Cr_3C_2 specimens had the highest TRS value (1821.2 MPa). As the sintering temperature was increased to 1300°C, in addition to excessive grain growth, the content of precipitated carbides also increased, which resulted in excessive hard and brittle strengthening phases in the matrix, and the TRS value was declined significantly (1727.2 MPa). In other words, adding a suitable amount of Cr_3C_2 powders to Ti-6Cu-8Nb alloys can effectively improve the mechanical properties after the vacuum sintering process. Hence, the 1275°C sintered – 5 Cr_3C_2 specimens possess the ideal hardness (67.8 HRA) and the highest TRS value (1821.2 MPa).

According to the above discussion and results, it is reasonable to conclude that the 1275°C sintered – 5 Cr_3C_2 specimens have optimal sintering characteristics and mechanical properties. Subsequent experiments will conduct microstructure analysis and corrosion testing on the Ti-6Cu-8Nb-xCr_3C_2 specimens using the optimal sintering temperatures (1275°C).

3.2. Effect of microstructure and corrosion behaviors on sintered Ti-6Cu-8Nb-xCr_3C_2 alloys

Fig. 4 displays the OM images of the various mass% Cr_3C_2, which were added to Ti-6Cu-8Nb alloys after sintering at 1275°C for 1 h. It can be observed that when 1 mass% Cr_3C_2 was added, there were still elongated flaky α-phases with staggered distribution in the β-phase matrix (as seen in Fig. 4a). At the same time, the discontinuous and coarse α-phase precipitated from the β grain boundaries. When the Cr_3C_2 was increased to 3 mass%,

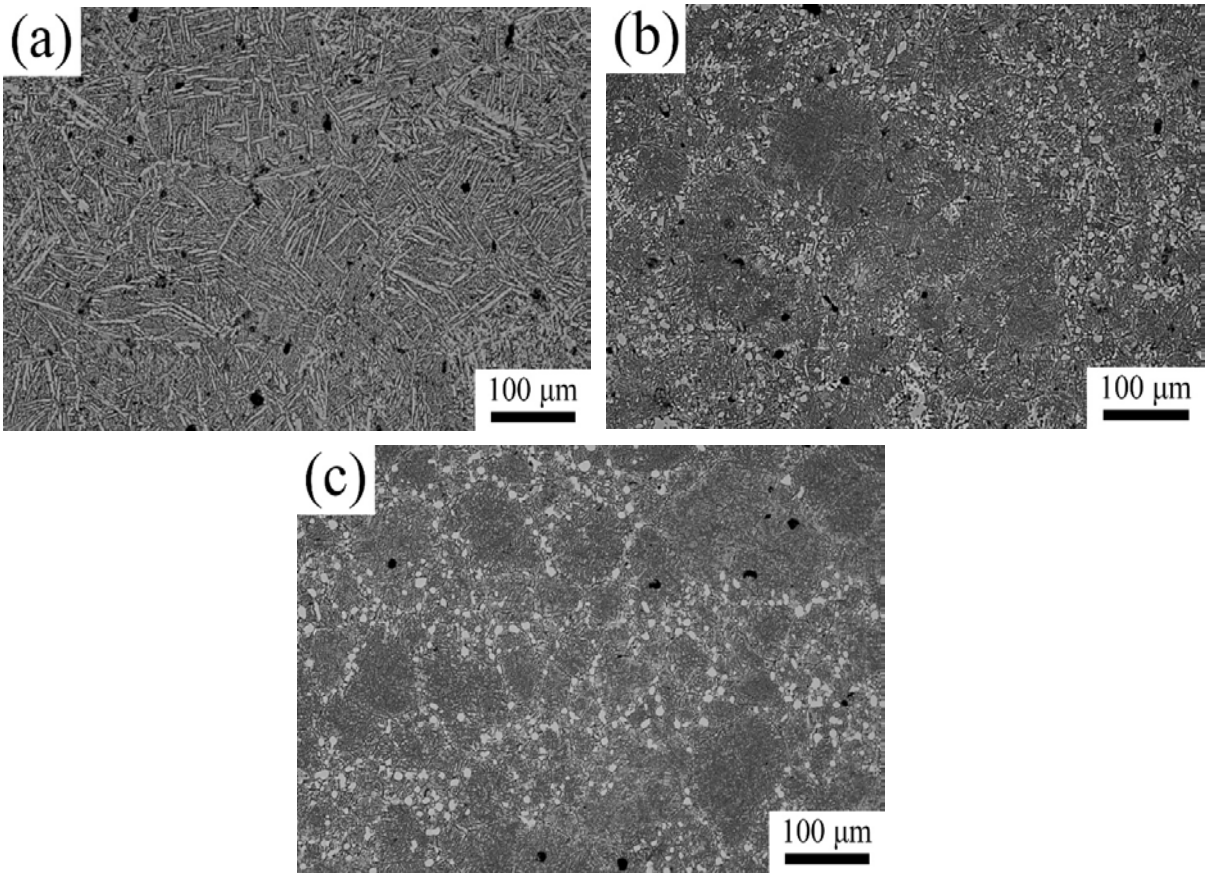

Fig. 4. The OM images of various mass% Cr_3C_2 added to Ti-6Cu-8Nb alloys after sintering at 1275°C for 1 h. (a) 1 Cr_3C_2, (b) 3 Cr_3C_2, and (c) 5 Cr_3C_2

there was a refining phenomenon of grain size, as shown in Fig. 4b. Moreover, when the flaky α-phase located on the grain boundaries became more slender, the α-phase in the β-phase matrix became less obvious. This result supports and is coherent with the previous XRD analysis, meaning that the higher Cr_3C_2 content will cause the diffraction peak of the β-phase to have stronger intensity, while the diffraction peak of the α-phase will have weaker intensity.

It is worth noting that, as the content of Cr_3C_2 was increased, more carbide particles were found to precipitate on the grain boundaries, as shown in Fig. 4c. This means that when more Cr_3C_2 powders are added, the chance of an in situ reaction of Cr_3C_2 increases significantly. Actually, 1 mole of Cr_3C_2 can reduce 3 moles of Cr, thus, the more Cr_3C_2 is added (5 mass%), the more Cr is reduced. As the diffusion rate of Cr in β-Ti is about 4 to 5 times that of the self-diffusion of Ti [24], it is much higher than that of Nb, thus, it can fill the pores produced by Nb in Ti alloys. In other words, adding a high content of Cr_3C_2 is conducive to improving the degree of densification. All the phase distributions of Ti-6Cu-8Nb-xCr_3C_2 alloys will be further examined by subsequent EBSD analysis.

Fig. 5a reveals the low-magnification SEM images of Ti-6Cu-8Nb-5Cr_3C_2 alloys after sintering at 1275°C for 1 h. The EDS analysis results are shown in TABLE 1. Further observation of the 1275°C sintered – 5 Cr_3C_2 specimens by high-magnification SEM are shown in Fig. 5b. The constituent elements of locations a-1 and b-1 are the solid-solution phases of Ti and Nb. It is speculated that the precipitates could be the flaky α-phase. According to the above XRD analysis, the intensity of the diffraction peak of the β-phase mainly depends on the content of Cr_3C_2, and as the content of Cr_3C_2 increases, more Cr atoms are produced by the in situ reduction of Cr_3C_2. As a result, locations 5a-2 and 5b-2 are composed of Ti, Cu, Nb, and Cr elements, respectively. Since Nb is a β-phase stable element, it is reasonable to surmise that this precipitate is likely to be β-phase.

As seen in TABLE 1, the compositions of locations 5a-3 and 5b-3 are Ti and C elements, respectively. Among them, titanium accounts for 51.29 at% and carbon accounts for 48.71 at% (location 5a-3); therefore, as the composition ratio of the two elements is almost 1:1, according to the preliminary judgment, the precipitates could be TiC. Notably, the compositions of locations 5a-4 and 5b-4 are Ti, Nb, and C elements, respectively, and this finding may be related to the NbC observed in previous XRD analysis. Subsequent analysis will utilize EPMA to check the element distribution, while EBSD will confirm the existence of TiC and NbC precipitates. In addition, the compositions of locations 5b-5 are Ti, Cu, Nb and Cr elements, respectively. Moreover, Ti accounts for 65.75 at%, while Cu accounts for 29.68 at%, meaning the Ti atom content is almost twice as much as Cu, thus, it is reasonable to judge that it may belong to the Ti_2Cu intermetallic compound. This EDS results also confirms the previous discussions of this study.

In addition to high hardness and high strength, the corrosion resistance of titanium alloys is another important property. Fig. 6 shows the Tafel slope results of 1275°C sintered – 1 Cr_3C_2, 3 Cr_3C_2 and 5 Cr_3C_2 specimens after 1 N H_2SO_4 corrosion testing. Notably, all the specimens possess a significant passivation phenomenon. A passivation layer will be produced on the material's surface, which can effectively protect the interior material,

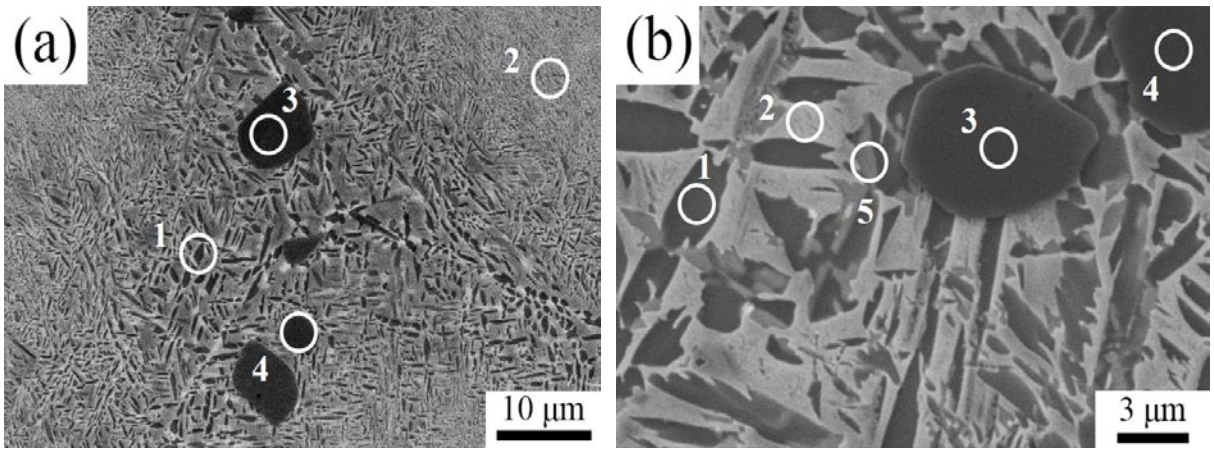

Fig. 5. The SEM images of Ti-6Cu-8Nb-5Cr_3C_2 alloys after sintering at 1275°C for 1 h: (a) low-magnification, and (b) high-magnification images

TABLE 1

The EDS analysis of the Figs. 5a and 5b

Elements (at%)	(a)-1	(a)-2	(a)-3	(a)-4	(b)-1	(b)-2	(b)-3	(b)-4	(b)-5
Ti	98.20	81.57	51.29	52.48	97.05	81.02	54.39	48.25	65.75
Cu	—	4.24	—	—	—	4.32	—	—	29.68
Nb	1.80	8.99	—	1.15	2.95	8.93	—	1.72	3.44
Cr	—	5.20	—	—	—	5.73	—	—	1.13
C	—	—	48.71	46.37	—	—	45.61	50.03	—

thereby improving the corrosion resistance. This result indicates that the sintered-Ti-6Cu-8Nb-xCr_3C_2 specimens have excellent corrosion resistance. Generally speaking, in an electrochemical reaction, the current value represents the diversification of the equilibrium constants in the oxidation reaction; if the current value is high, it leads to rapid oxidation. Previous literature indicates that Cr_3C_2 itself has good corrosion resistance [19-21]. Moreover, adding Nb and Cr elements to the Ti alloy can strengthen the passivation film of the Ti-based alloys. In this work, the Nb and Cr elements are uniformly dissolved in the titanium substrate to help improve corrosion resistance. According to the above discussion, the addition of an appropriate amount of Cr_3C_2 is helpful to improve the microstructure, as it decreases the oxidation rate. This study further investigated the corrosion resistance of the sintered-Ti-6Cu-8Nb-xCr_3C_2 specimens. Although the Tafel slope result of the specimens did not display an obvious variation, the increase in the amount of Cr_3C_2 led to a corrosion current rise and decline ($3.34 \rightarrow 3.71 \rightarrow 3.61 \times 10^{-5}$ A·cm^{-2}). This study also considered polarization resistance, as higher polarization resistance usually means better corrosion resistance [3,20]. As the added Cr_3C_2 content was increased, the polarization resistance slightly increased ($4.34 \rightarrow 4.63 \rightarrow 4.84 \times 10^3$ Ω·cm^2). According to the results, the 5 Cr_3C_2 specimens had the highest polarization resistance value and good corrosion current, meaning the optimal corrosion resistance.

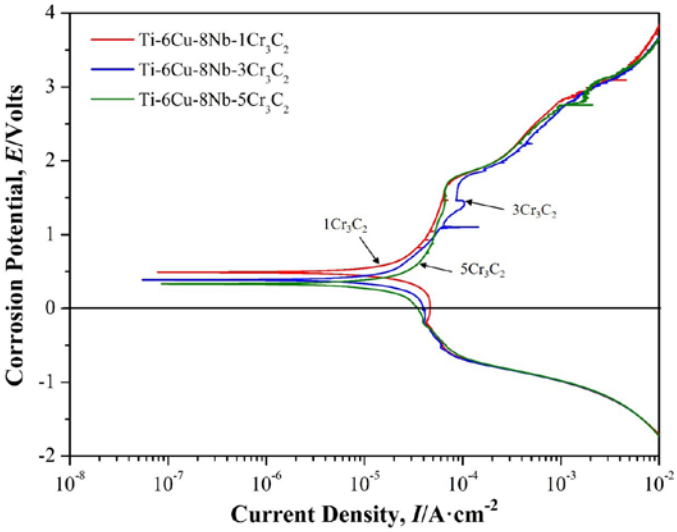

Fig. 6. Tafel results of various mass% Cr_3C_2 added to Ti-6Cu-8Nb alloys after sintering at 1275°C for 1 h

3.3. Effect of phase distribution and crystal orientation on sintered Ti-6Cu-8Nb-xCr_3C_2 alloys

According to the X-ray and microstructure analysis conducted in this paper, TiC and NbC precipitates appeared in the Ti-6Cu-8Nb-xCr_3C_2 alloy. In order to further judge whether or not the precipitates were TiC and NbC, and to understand the phase distribution ratio and crystal orientation in the Ti-6Cu-8Nb-xCr_3C_2 alloy, subsequent research used EPMA and EBSD analysis for the 1275°C sintered Ti-6Cu-8Nb-xCr_3C_2 specimens. Taking the 1275°C sintered – 5 Cr_3C_2 (Ti-6Cu-8Nb-5Cr_3C_2) specimens as an example, the EPMA and EBSD analysis of different additions of Cr_3C_2 revealed similar results.

Fig. 7 represents the EPMA analysis of the element distributions for the 5 Cr_3C_2 specimens after sintering at 1275°C for 1 h. It can be found that the areas with higher concentrations of Ti and Cu are mainly the Ti_2Cu intermetallic compounds, as shown in Figs. 7b and 7c. This means that the two elements underwent eutectoid reaction to generate the second phase during the sintering process. The Ti_2Cu particles were mainly precipitated from the supersaturated α-phase, and distributed near the grain boundaries where the α-phase is located, while the reaction can be ascribed to α (supersaturation) → α + Ti_2Cu. On the other hand, as the β-phase in the grain inhibited the precipitation of the α-phase during the cooling process, it led to the refinement of the structure, and the precipitated particles of Ti_2Cu were smaller. In addition, it can be known from the BEI image (Fig. 7a) that there are some elements larger than the atomic weight of Ti in the β-phase, thus, it can be judged that the bright area is the β-phase. Simultaneously, as shown in Figs. 7d and 7e, the Nb and Cr elements obviously tend to be distributed uniformly in the area where the β-phase is located. Notably, the C element is mainly concentrated in the carbides of the black particles, as seen in Fig. 7a and Fig. 7f. Furthermore, it can be observed that Ti and a small amount of Nb are also distributed in the area where the C element is located, thus, it is reasonably inferred that the black particles (Fig. 7a) may be TiC and NbC or *M*C-type ((Nb, Ti)C) carbides.

Fig. 8 shows the phase distribution of EBSD analysis for 5 Cr_3C_2 specimens after 1275°C sintering for 1 h. Fig. 8a shows the image quality and Fig. 8b shows the phase mapping, respectively. As seen in Fig. 8b, obvious α-Ti, β-Ti, Ti_2Cu, TiC, and NbC signals appeared. Since the TiC and NbC have the same lattice type (NaCl structure), and similar atomic radius (1.47 Å and 1.46 Å), it is possible to generate a solid-solution reaction. Furthermore, the Ti_2Cu precipitates are located around the α-phase and display uniform distribution, while the needle-like α-phase is evenly dispersed in β-phase. The results of EBSD analysis of the structure distribution ratio for the Ti-6Cu-8Nb-5Cr_3C_2 alloys after 1275°C sintering for 1 h are shown in TABLE 2, where zero is the position distribution ratio of no signal in the image. As the added Cr_3C_2 increases to 5 mass%, the content of β-phase is significantly increased (12.24% -37.95%). While, TiC (4.44%) and NbC (8.04%) are mainly precipitated in the form of a composite structure, the carbide particles have become significantly smaller, and this result is coherent with the previous discussion of this paper.

The crystal orientation map (COM) of the EBSD analysis for the 1275°C sintered – 5 Cr_3C_2 specimens is shown in Fig. 9. All the Ti-6Cu-8Nb-xCr_3C_2 samples show the α-Ti of the HCP structure, and whether it is large-scale flakes or fine needle-like structures, they all have different crystal orientations. Simultaneously, it can be observed in the crystal orientation map that the β-Ti of the BCC structure had different color blocks, and that is

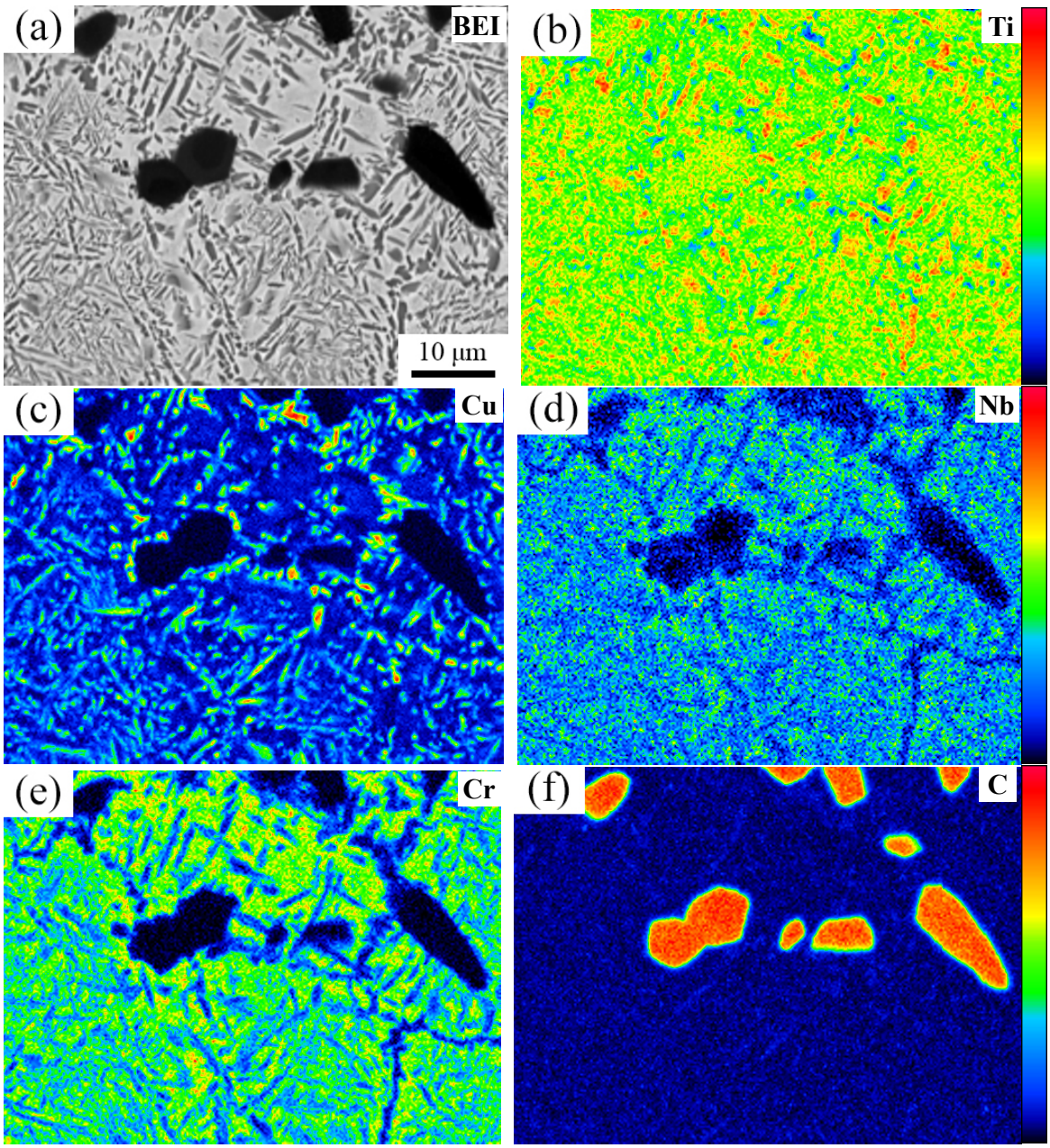

Fig. 7. EPMA-Mapping analysis of the elements distribution for Ti-6Cu-8Nb-5Cr_3C_2 alloys after sintering at 1275°C for 1 h: (a) BEI image, (b) Ti, (c) Cu, (d) Nb, (e) Cr, and (f) C

TABLE 2

EBSD analysis of the structure distribution ratio for Ti-6Cu-8Nb-5Cr_3C_2 alloys after sintering at 1275°C for 1 h (Hit Rate 98.25%)

Phase Name	α-Ti	β-Ti	Ti_2Cu	TiC	NbC	Zero
Phase Fraction (%)	37.07	37.95	10.75	4.44	8.04	1.75

the location of the grain distribution (Fig. 9b). Moreover, there is a continuous α-phase precipitation at the grain boundaries, as shown in Fig. 9a. In addition, Fig. 9b displays 6 different color blocks, which represent the 6 crystal grains in this crystal orientation map. In this analysis, the mean grain size of 5 Cr_3C_2 is significantly smaller than the 1 Cr_3C_2 and 3 Cr_3C_2 specimens. In other words, increasing the content of Cr_3C_2 powders (1 → 3 → 5 mass%) indeed has the effect of inhibiting grain growth, which is coherent with the previous discussion of this paper. It is worth noting that the second phase precipitates of the Ti_2Cu, TiC, and NbC structures also show no specific crystal orientation, as shown in Figs. 9c, 9d and 9e. This result confirms that the precipitates produced under the PM process do not have the problem of directionality. As previously mentioned, TiC and NbC will generate the *M*C-type carbides through the solid-solution reaction, thus, they have the same crystal orientation. In addition, it can be observed that, although TiC is mainly distributed on large carbide particles, as the solid solubility of carbon in the Ti alloys is only 0.2%, only a small amount of TiC is uniformly dispersed within β-Ti.

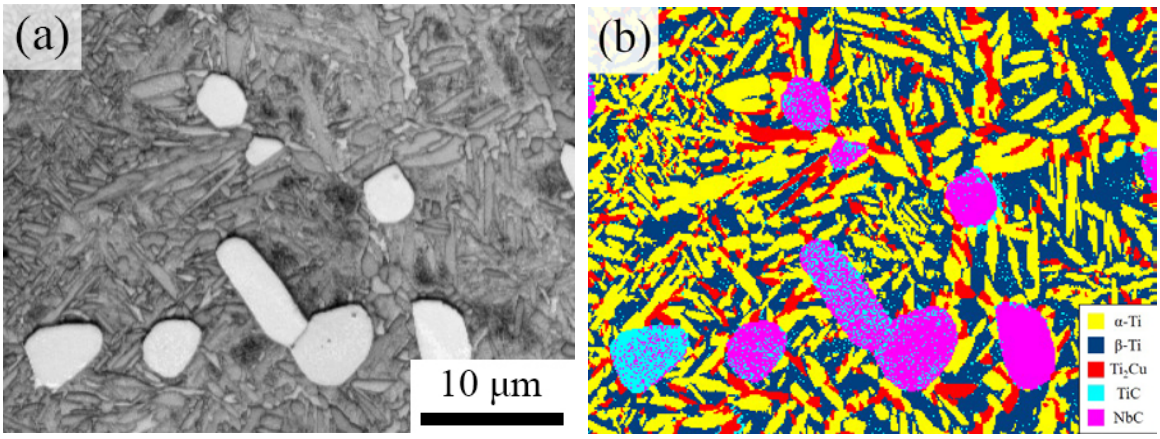

Fig. 8. The EBSD analysis for Ti-6Cu-8Nb-5Cr_3C_2 alloys after sintering at 1275°C for 1 h: (a) image quality, and (b) phase mapping, respectively

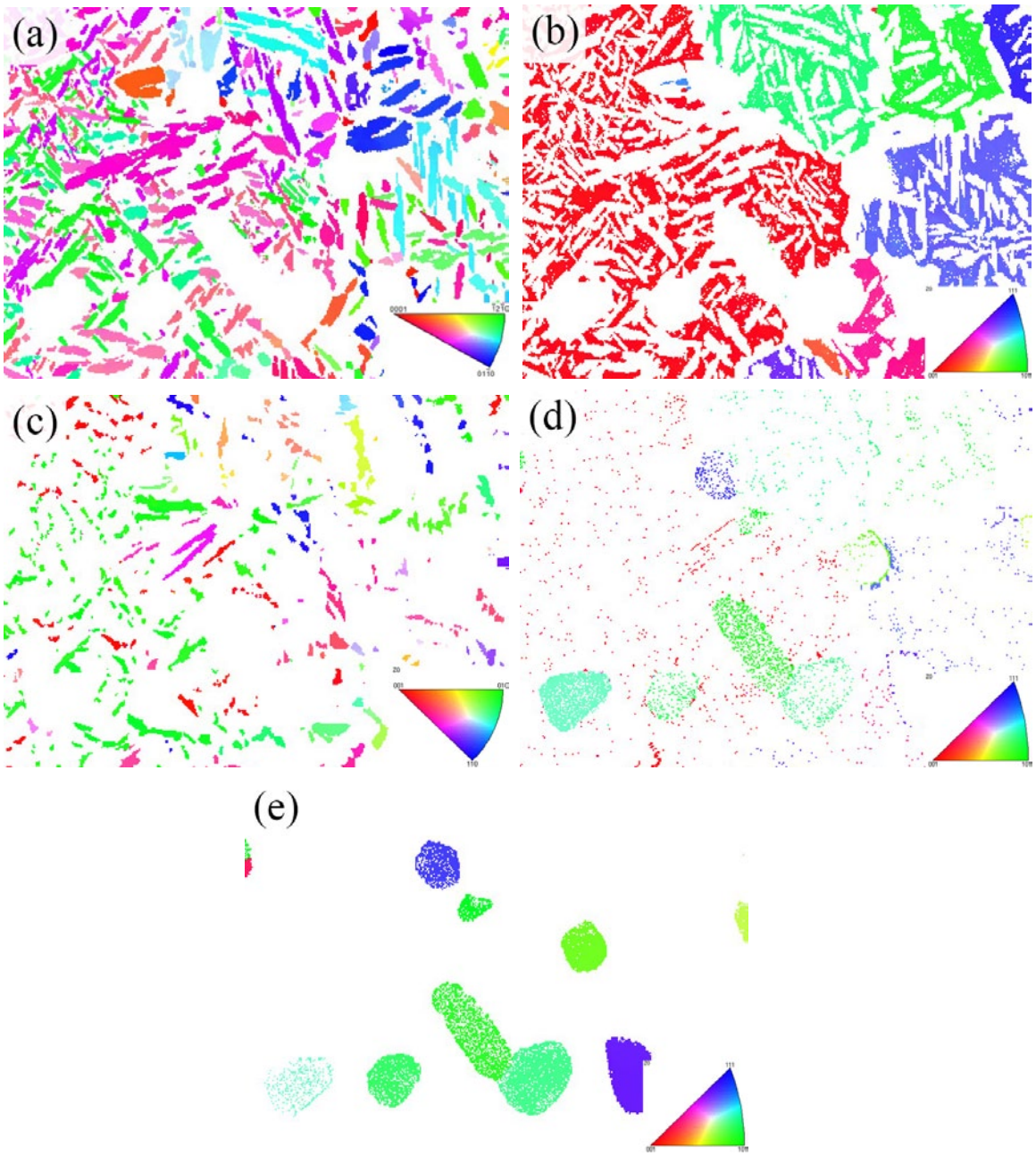

Fig. 9. The crystal orientation map of the EBSD analysis for Ti-6Cu-8Nb-5Cr_3C_2 alloys after sintering at 1275°C for 1 h: (a) α-Ti , (b) β-Ti, (c) Ti_2Cu, (d) TiC, and (e) NbC, respectively

EPMA of the element distribution and EBSD of the phase structure analysis proves that the reduced Cr atoms have been used as β-Ti stable elements and as a solid-solution in the Ti-6Cu-8Nb-5Cr_3C_2 alloy matrix. At the same time, by stabilizing β-Ti and inhibiting the precipitation of the α-phase, the microstructure of 5 Cr_3C_2 specimens can form a refined basket structure. Actually, during the vacuum sintering process, an in situ synthesis reaction occurred between Ti, Nb, and C, and the reaction equation is, as follows:

$$\text{Ti} + \text{C} = \text{TiC},\ \Delta G_T^{\theta} = -186731 + 13.2T\ (\text{J/mol}),\quad 298\ \text{K} \le T \le 2000\ \text{K} \tag{1}$$

$$\text{Nb} + \text{C} = \text{NbC},\ \Delta G_T^{\theta} = -140582 + 5.732T\ (\text{J/mol}),\quad 298\ \text{K} \le T \le 3500\ \text{K} \tag{2}$$

where ΔG_T^{θ} is the Gibbs free energy and T is the temperature. It can be found from the above formula that the free energy of TiC is lower than that of NbC, which means that TiC will be generated first. However, the ratio between Ti and Nb will affect the free energy gap between the two elements, which has significant effect on the formation of (Nb, Ti) C. When the sintering temperature increases, the free energy gap between TiC and NbC becomes smaller, which gradually increases the nucleation ability of NbC, thus, it is reasonable to surmise that the TiC will be preferentially generated, and can be used as a heterogeneous nucleation point for NbC precipitation. Consequently, the formation of TiC will promote the precipitation of NbC, and the *M*C-type carbide of (Nb, Ti) C is produced under the continuous cycle of precipitation [25], and this finding is consistent with EPMA and EBSD analysis.

According to above the discussion and results, the microstructure of vacuum sintering Ti-6Cu-8Nb-xCr_3C_2 alloys possesses both α and β-phase structures, as well as various Ti_2Cu, TiC, and NbC precipitates. This finding is coherent with our previous studies [2,3]. It is possible that the main strengthening mechanisms of vacuum sintering Ti-6Cu-8Nb-xCr_3C_2 alloys include dispersion strengthening, solid-solution strengthening, and precipitation hardening. Moreover, the sintering mechanism and properties of the Ti-6Cu-8Nb alloy were effectively improved by adding a suitable amount of Cr_3C_2 powder through the vacuum sintering process.

4. Conclusions

This study found that increasing the amount of Cr_3C_2 is effective in reducing the apparent porosity of Ti-6Cu-8Nb alloys, which is beneficial to sintering densification. Moreover, adding 5 mass% Cr_3C_2 had the best effect on inhibiting grain growth. Therefore, the mechanical properties and corrosion resistance of the composite materials (Ti-6Cu-8Nb-xCr_3C_2) were obviously enhanced after adding the 5 mass% Cr_3C_2 powder to the Ti-6Cu-8Nb alloy. The 5 Cr_3C_2 specimen possessed suitable hardness (67.8 HRA) and the greatest TRS value (1821.2 MPa) after sintering at 1275°C for 1 h; while the 5 Cr_3C_2 specimen also had the optimal corrosion resistance (polarization resistance was $4.84 \times 10^3\ \Omega\cdot\text{cm}^2$).

Comparison of the Ti-6Cu-8Nb alloy found that the hardness and TRS of the Ti-6Cu-8Nb-5Cr_3C_2 alloy increased by about 8% (62.8 → 67.8 HRA) and 20% (1517.6 → 1821.2 MPa), respectively. Moreover, XRD analysis proved that the in situ reduction reaction of $Cr_3C_2 + 2Ti \rightarrow 2TiC + 3Cr$ occurred through the vacuum sintering process. In addition, EPMA and EBSD results show that the α, β, Ti_2Cu, TiC, and NbC phases are present in the 1275°C sintered- Ti-6Cu-8Nb-xCr_3C_2 alloy matrix. Consequently, it can be concluded that the microstructure evolution of a vacuum sintered Ti-6Cu-8Nb-xCr_3C_2 alloy on strengthening characteristics can be ascribed to the dispersion strengthening, solid-solution strengthening, and precipitation hardening of the multiple strengthening mechanisms.

Acknowledgments

This research is supported by the Ministry of Science and Technology of the Republic of China under Grant No. **MOST 109-2221-E-027-062-**. The authors would like to express their appreciations for ASSAB STEELS TAIWAN CO., LTD. Furthermore, thanks to Prof. H.C. Lin and Mr. C.Y. Kao of Instrumentation Center, National Taiwan University for EPMA and EBSD experiments.

REFERENCE

[1] J.L. Hu, H.X. Li, X.Y. Wang, L. Yang, M. Chen, R.X. Wang, G.W. Qin, D.F. Chen, E.L. Zhang, Materials Science & Engineering C **115**, 110921 (2020).

[2] K.T. Huang, S.H. Chang, H.T. Wang, Materials Transactions **58**, 1581-1586 (2017).

[3] S.H. Chang, L.Y. Hung, T.H. Yang, Materials Chemistry and Physics **235**, 121743 (2019).

[4] B. Callegari, J.P. Oliveira, R.S. Coelho, P.P. Brito, N. Schell, F.A. Soldera, F. Mücklich, M.I. Sadik, J.L. García, H.C. Pinto, Materials Characterization **162**, 110180 (2020).

[5] J.P. Oliveira, B. Panton, Z. Zeng, C.M. Andrei, Y. Zhou, R.M. Miranda, F.M. Braz Fernandes, Acta Materialia **105**, 9-15 (2016).

[6] B. Callegari, J.P. Oliveira, K. Aristizabal, R.S. Coelho, P.P. Brito, L. Wu, N. Schell, F.A. Soldera, F. Mücklich, H.C. Pinto, Materials Characterization **165**, 1100400 (2020).

[7] J.W. Wang, S.Y. Zhang, Z.Q. Sun, H. Wang, L. Ren, K. Yang, Journal of Materials Science and Technology **35**, 2336-2344 (2019).

[8] Y. Alshammari, F. Yang, L. Bo, Journal of the Mechanical Behavior of Biomedical Materials **95**, 232-239 (2019).

[9] S.M. Javadhesari, S. Alipour, M.R. Akbarpour, Colloids and Surfaces B **189**, 110889 (2020).

[10] I. Çaha, A.C. Alves, P.A.B. Kuroda, C.R. Grandini, A.M.P. Pinto, L.A. Rocha, F. Toptan, Corrosion Science **167**, 108488 (2020).

[11] D. Kalita, Ł. Rogal, P. Bobrowski, T. Durejko, T. Czujko, A. Antolak-Dudka, E. Cesari, J. Dutkiewicz, Materials **13**, 2827 (2020).

[12] D. Kalita, Ł. Rogal, T. Czeppe, A. Wójcik, A. Kolano-Burian, P. Zackiewicz, B. Kania, J. Dutkiewicz, Journal of Materials Engineering and Performance **29**, 1445-1452 (2020).

[13] E. Yılmaz, A. Gökçe, F. Findik, H.O. Gulsoy, O. İyibilgin, Journal of the Mechanical Behavior of Biomedical Materials **87**, 59-67 (2018).

[14] E. Yılmaz, A. Gökçe, F. Findik, H. Gulsoy. Journal of Alloys and Compounds **746**, 301-313 (2018).

[15] E. Yılmaz, A. Gökçe, F. Findik, H.Ö. Gülsoy, Vacuum **142**, 164-174 (2017).

[16] S.H. Chang, G.L. Huang, K.T. Huang, Powder Metallurgy **63**, 104-115 (2020).

[17] K.T. Huang, S.H. Chang, P.C. Hsien, Journal of Alloys and Compounds **712**, 760-767 (2017).

[18] M. Yi, X.Z. Zhang, G.W. Liu, B. Wang, H.C. Shao, G.J. Qi, Materials Characterization **140**, 281-289 (2018).

[19] M. Chen, X. Xiao, X.F. Zhang, C.Y. Zhao, Materials Research Express **6**, 076533 (2019).

[20] S.H. Chang, K.Y. Lee, K.T. Huang, T.H. Yang, Kovove materialy-Metallic Materials **57**, 317-327 (2019).

[21] H.X. Tian, M.Y. Zhang, Y.B. Peng, Y. Du, P. Zhou, International Journal of Refractory Metals **78**, 240-246 (2019).

[22] S.H. Chang, C.Y. Chuang, K.T. Huang, ISIJ International **59**, 1354-1361 (2019).

[23] Q.T. Li, Y.P. Lei, H.G. Fu, Applied Surface Science **316**, 610-616 (2014).

[24] H.C. Hsu, S.C. Wu, T.Y. Chiang, W.F. Ho, Journal of Alloys and Compounds **476**, 817-825 (2009).

[2] Y.C. Zhang, R.B. Song, Y. Pei, E. Wen, Z.Y. Zhao, Journal of Alloys and Compounds **824**, 153806 (2020).